Self-templated 3D Sulfide-based Solid Composite Electrolyte for Solid-State Sodium Metal Batteries

Xiaolin Guo,[a] Yang Li,[a] Selim Halacoglu,[a] Kincaid Graff,[b] Chunyan Zhang,[c] Kelvin Fu,[c] Claire(Hui) Xiong,[b] Hui Wang*[a]

a. Mechanical Engineering Department, University of Louisville, US, 40292
b. Micron School of Materials Science and Engineering, Boise State University, USA, 83725
c. Mechanical Engineering Department, University of Delaware, US, 19716

Corresponding Author: hui.wang.1@louisville.edu

Abstract

Rechargeable solid-state sodium metal batteries (SSMBs) experience growing attention owing to the increased energy density (*vs.* Na-ion batteries) and cost-effective materials. Inorganic sulfide-based Na-ion conductors also possess significant potential as promising solid electrolytes (SEs) in SSMBs. Nevertheless, due to the highly reactive Na metal, poor interfaces compatibility is the biggest obstacle for inorganic sulfide solid electrolytes such as Na_3SbS_4 to achieve high performance in SSMBs. To address such electrochemical instability at interface, new design of sulfide SE nanostructures and interface engineering are highly essential. In this work, we report a facile and straightforward approach to prepare three-dimensional (3D) sulfide-based solid composite electrolytes (SCEs), which utilizes porous Na_3SbS_4 (NSS) as a self-templated framework and fill with a phase transition polymer. The 3D structured SCEs displays obviously improved interface stability toward Na metal than pristine sulfide. The assembled SSMBs (with TiS_2 or FeS_2 as cathodes) deliver outstanding electrochemical cycling performance. Moreover, the cycling of high-voltage oxide cathode $Na_{0.67}Ni_{0.33}Mn_{0.67}O_2$ (NNMO) is also demonstrated in SSMBs using 3D sulfide-based SCEs. This study presents a novel design on self-templated nanostructure of SCEs, paving the way for the advancement of high-energy sodium metal batteries.

Keywords: Self-template; Na-ion conductor; Sulfide; Solid composite electrolyte; Sodium metal batteries

1. Introduction

In the past few decades, solid-state batteries (SSBs) have garnered intense attention owing to the improved energy density and safety than the conventional batteries with liquid electrolytes.[1] The adoption of sodium (Na) electrochemistry enables the solid-state technology for medium- or grid-scale energy storage systems due to the cost-effective materials and abundant resources.[2] Specifically, metallic Na anode is attractive due to its high specific capacity (1,166 mA h g^{-1}) and good electrochemical potential vs lithium.[3-5] In solid-state sodium metal batteries, the optimal solid electrolytes (SEs) are expected to hold features such as (1) high ionic conductivity, (2) chemical and electrochemical stability toward electrodes (anode and cathode). So far, the most popular inorganic Na-ion conductors are classified into oxides (β-Al_2O_3,[6] $Na_3Zr_2Si_2PO_{12}$[7-8]), sulfides (Na_3PS_4,[9] Na_3SbS_4,[10] $Na_{11}Sn_2PS_{12}$[11]), halides ($Na_{3-x}Y_{1-x}Zr_xCl_6$,[12] $Na_2Y_{2/3}Cl_4$,[13] $Na_{3-x}Er_{1-x}Zr_xCl_6$[14]), etc.

Inorganic sulfide Na-ion conductors emerged as promising SEs for SSMBs due to their advantages of impressive ionic conductivity (> 10^{-4} S cm^{-1}), ductile properties and cold-press densification.[15] Na_3SbS_4 (NSS) is a representative sulfide SEs, and has attracted considerable research interests on the synthesis, doping chemistry, electrochemical stability, as well as battery demonstration.[10, 16-18] Nevertheless, the previous studies report that NSS also suffers from some common issues that occur on sulfide SEs, specifically the interface stability toward alkali metal and oxide cathodes.[19-20] Moreover, the large interface resistance that originated from poor solid/solid contact also results in unsatisfied battery cycling performance. To address these challenges in SSMBs, interface engineering has been employed to stabilize the electrode/SE interface by introducing either artificial interlayer or self-formed interlayer. [21-23]

For examples, the interfacial compatibility between solid electrolytes and sodium metal could be greatly improved by utilizing Cl- and Br- doped NSS as the electrolyte comparing to pure NSS.[24-25] To stabilize the Na/NSS interface, Yao et al [19] introduced an electron-blocking cellulose-poly(ethylene oxide) interlayer and Sun et al [26] employed an alucone film on sodium metal surface by molecular layer deposition method. Our group reported that poly(ethylene glycol)-block-poly(propylene glycol)-block-poly(ethylene glycol)/NaTFSI (PEG-PPG-PEG, PPP) as a compatible interlayer between NSS and sodium metal.[27] Besides, engineering the components of SEs such as solid composite electrolyte (SCE) could be a promising approach to address the above challenges. Many studies have focused on the polymer-rich composite electrolytes.[28-29]

The "polymer-in-ceramic" composite (also called "ceramic-rich" composite) design is considered a viable and efficient strategy to modify the interface while remain sufficient stiffness, contributing to high performance batteries.[30] Different synthetic approaches have been explored to prepare the ceramic-rich composite with polymers. One of the most popular methods is the solvent-assist method, which requires to involve the selected polar or nonpolar solvents (e.g., tetrahydrofuran (THF), dimethylformamide (DMF), acetonitrile (ACN)) to disperse/dissolve precursors (ceramic, polymers).[30-31] This method is simple and straightforward, nevertheless, the solvent-processing may cause the dramatic decrease of ionic conductivity ceramic conductors after the drying treatment.[32] An alternative solvent-free approach is to leverage small amount of binder materials such as polytetrafluoroethylene (PTFE) to fabricate SE membranes.[33-34] Recently, a template method has been examined to successfully prepare ceramic-dominant SCEs. For instance, sacrifice templates such as SeS_2,[35]

graphite[36] and poly(vinyl alcohol) (PVA)[37] are introduced to ceramic materials to form the desired structure of ceramic, and are removed by the following high temperature sintering. However, the sacrificial template method not only needs the additional heating treatment but also requires very stringent synthetic conditions to avoid the residual impurity to devastate the ionic conductivity. Therefore, it is more desirable to explore novel synthetic approaches such as self-template method to prepare ceramic-rich SCEs for solid-state Na batteries.

In this work, we design and demonstrate to use inorganic NSS with 3D porous framework as a self-template to infiltrate a phase transition polymer (PEG-PPG-PEG, named as PPP) to prepare 3D structured SCEs for SSMBs. As shown in **Scheme 1**, the 3D porous NSS pellet is first obtained by heating the hydrate to an elevated temperature to remove the hydrate water, and then infiltrated with a phase transition polymer (PPP/NaTFSI), followed by cooling down to produce 3D structured NSS/PPP SCEs. With such structure and composition design, the 3D-NSS/PPP SCE exhibits distinctively better interface stability toward Na metal in the symmetric cell cycling. In addition, the assembled SSMBs (TiS_2|3D-NSS/PPP SCE|Na) show an initial discharge capacity of 176.3 mA h g^{-1} under a current density of 50 mA g^{-1} and remain stable cycling up to 550 cycles. Moreover, the cycling ability of 3D-SCE based SSMBs with oxide cathode $Na_{0.67}Ni_{0.33}Mn_{0.67}O_2$ (NNMO) up to 4.0V is also demonstrated to display discharge capacity of 82 mA h g^{-1} at 0.1 C without external pressure. This research provides a new design on self-templated sulfide-based SCEs and demonstrate their great potentials for high energy solid-state Na metal batteries.

2. Experimental Section

2.1. Materials Synthesis

The 3D porous NSS was synthesized by a facile method. The NSS hydrate powder[38] was first cold pressed to a pellet under the pressure of ~300 MPa. Subsequently, the NSS hydrate pellet will transform into 3D porous NSS pellet after vacuum heat-treatment at 150 ˚C for 1.5 h, then 300 ˚C for 1h. The conductive polymer was prepared by dissolving 3.0313 g NaTFSI salt (sodium bis(trifluoromethanesulfonyl)imide, Alfa Aesar 99.999%) into 10 mL PPP (PEG-PPG-PEG, Sigma-Aldrich, Mn~5800) at 60 ˚C. Due to the high viscosity of the conductive polymer, the conductive polymer permeates into 3D porous NSS pellet with vacuum assisted to make sure the polymer penetrating inside pores of the 3D pellet. The infiltrating process was conducted for several times in the glovebox under the protection of Argon atmosphere.

2.2. Materials Characterization

The samples were characterized by X-ray diffraction (XRD, Bruker Discovery D8 HR-RDS, nickel filtered Cu Kα radiation, λ=1.5418 Å) to confirm the phase in the 2θ range of 10 - 80˚. Raman scattering spectra were collected by a Renishaw inVia Raman/PL Microscopy with a wavelength of 632.8 nm laser. The surface and cross-sectional morphology and related chemical elements distribution were characterized by a scanning electron microscopy (SEM, TESCAN Vega3) combined with an energy-dispersive X-ray spectrometry (EDS) detector. To determine the content ratio of NSS and PPP polymer electrolyte in 3D-NSS/PPP SCE, TGA characterizations were performed using Q600 SDT under nitrogen atmosphere from room temperature to 550 ˚C. In addition, the direct weighting method was also employed to record the mass weight before and after PPP polymer incorporation. The results from direct weighting

method are shown in Table S1. The weight before and after polymer incorporation is 99.5 mg, and 145.3 mg, respectively. Thus, the polymer content is estimated to be 33 wt%, and NSS content is 67 wt%. Fourier Transform Infrared Spectroscopy (FTIR) spectra were collected via PerkinElmer Spectrum BX FTIR system using excitation laser source of 633 nm.

2.3. Electrochemical Measurements

The ionic conductivity of 3D-NSS/PPP composite was evaluated in 2032-coin cells with carbon coated aluminum as the blocking electrode. The electrochemical impedance spectroscopy (EIS) measurements were tested using the potentiostat (Biologic VSP300) in the frequency range of 5 MHz to 0.1 Hz. The ionic conductivity was calculated by $\sigma = L/(A \times R)$, where σ refers to the ionic conductivity (S cm^{-1}), L is the pellet's thickness (500-600 micrometer), A is the area (cm^2), R is the impedance from Nyquist plots (Ω). The Arrhenius plots were obtained by measuring the conductivity of 3D-NSS/PPP in the range of 30 to 80 °C. The activation energy could be calculated by fitting the Arrhenius plot based on the equation: $\sigma = \sigma_0 \exp\left(-\frac{E_a}{kT}\right)$, where σ, σ_0, E_a, k, and T are ionic conductivity, pre-exponential factor, activation energy, Boltzmann constant and Kelvin temperature, respectively.[29] Sodium ion transference number (t_{Na^+}) was tested with a direct current (DC) polarization with the structure of Na|3D-NSS/PPP|Na symmetric cell and calculated based on the Bruce-Vincent equation: $t_{Na^+} = \frac{I_{ss}(\Delta V - I_0 R_0)}{I_0(\Delta V - I_{ss} R_{ss})}$, where I_0 and I_{ss} are the initial and steady currents, ΔV is the polarization voltage (10 mV), R_0 and R_{ss} are the charge-transfer impedance of the symmetric cell before and after polarization, respectively.[29] The Linear Sweep Voltammetry (LSV) method was employed to measure the electrochemical window in Na||SS cell (SS: stainless steel) with the scanning rate is 1 mV s^{-1}. The symmetric cell (Na|3D-NSS/PPP|Na) cycling was studied under a current density of 0.1

mA cm^{-2} (energy density of 0.05 mA h cm^{-2}).

2.4. Electrochemical Cycling in SSMBs.

Three different active cathode materials (TiS_2, FeS_2, and $Na_{0.67}Ni_{0.33}Mn_{0.67}O_2$) were employed for the assembly of SSMBs, respectively. For the cathode preparation, TiS_2 (99.8%, Strem Chemicals) acetylene black and PVDF binder were mixed in the mass ratio of 60:30:10 to form a homogeneous slurry. Similar preparation is applied for FeS_2 (99.9%, Alfa Asar) as the cathode. For the high-voltage P2-$Na_{0.67}Ni_{0.33}Mn_{0.67}O_2$ (NNMO) cathode,[39] the slurry was made by mixing the active material NNMO with Super P and PVDF binder with a weight ratio of 80:10:10. Then, the slurry was coated on the aluminum foil and subsequently dried vacuum oven at 80 ˚C for overnight. For all prepared cathodes, the active materials mass loading was about 1 mg cm^{-2}. The all-solid-state batteries were assembled with 2032-coin cell inside of Argon-filled glovebox (H_2O and O_2 content are both below 0.1 ppm). The assembled SSMBs were tested on the NEWARE battery testing system for further galvanostatic cycling and rate performance measurements at the temperature of 55 ˚C within different voltage windows: 1.4-3 V for TiS_2, 0.9-3 V for FeS_2, 2-4 V for NNMO. The cycled Na|3D-NSS/PPP|NNMO cell were disassembled for further analysis at interface. X-ray photoelectron spectroscopy (XPS) spectra was recorded using Thermo VG Scientific ESCALAB XI X-ray photoelectron spectrometer microprobe. The surface of NNMO cathode before and after cycling was characterized by time-of-flight secondary-ion mass spectrometry (TOF-SIMS, IONTOF) over a 100 x 100 μm^2 raster size, and the mass range is fixed between 0 and 800 μm for secondary ions of Na^+, Ni^+ and Mn^+.

3. Results and Discussion

Figure 1a shows the X-ray diffraction (XRD) patterns of NSS hydrate pellet after heated at 150 and 300 °C, and then infiltrated PPP polymer. The heat-treated pellet samples show characteristic diffraction peaks at 2θ = 17.1, 30.2, and 35˚ for pure NSS, which are consistent with previous literatures.[10, 28, 40-42] No obvious changes on XRD patterns for the pellet samples after heating at 150 °C and 300 °C. Unlike the powder sample (Figure S1), NSS pellets show stronger peaks at lower 2θ range. After infiltration of PPP/NaTFSI, the synthesized NSS/PPP SCE pellet display strong diffraction peaks of NSS while minor bump (2θ = 22˚) originate from the polymer electrolyte, suggesting that the majority of PPP is located inside NSS pellet other than the surface. The Raman spectra (**Figure 1b**) show three strong peaks located at 360 and 382/401 cm^{-1} that originated from the symmetric and asymmetric stretching vibration of SbS_4^{3-}, respectively.[28, 42] Both XRD and Raman results indicate that NSS is chemically stable with PPP. Moreover, the Raman spectra at 600-1200 cm^{-1} range (Figure S2) displayed the characteristic peaks of PPP/NaTFSI (e.g. 740, 863 cm^{-1}) well remained in the NSS/PPP SCE. For the FTIR spectra (Figure S3), the NSS/PPP SCE display characteristics peaks from PPP/ NaTFSI (e.g., 2860, 1350, 1091 cm^{-1}) and NSS (e.g., 1430, 970 cm^{-1}), respectively.[43] This observation further confirms that there is no chemical bonding formation between NSS and PPP polymer electrolyte. TGA curves of 3D-NSS/PPP SCE and 3D-NSS are shown in **Figure 1c.** From room temperature to 550 °C, 3D-NSS pellet shows flat curve and remains 95% weight. In contrast, the 3D-NSS/PPP exhibits an obvious weight loss of 35 wt% between 360-380 °C and finally loses 68% after 500 °C. Such a large weight loss is due to the decomposition of PPP polymer electrolyte (Figure S4). From the TGA results, the NSS content is estimated to 68 wt%

and the polymer content is 32% wt%, which is in agreement with the results from direct weight measurement method (Table S1).

Figure 1d-f display the SEM images of heat-treated NSS pellet and NSS/PPP SCE pellet. Before heating treatment, the pressed hydrate pellet is smooth and relatively dense surface morphology with micro-cracks (Figure S5). In contrast, the heat-treated NSS pellet show obvious micro- and nano-sized pores on surface within a range of 0.2-5 μm. These pores are directly formed due to water removal during the heating process of hydrate sample other than insufficient cold-press densification. The cross-sectional SEM image (**Figure 1f**) further confirms the porous structure through the NSS pellet with a thickness of 500 μm. Moreover, the corresponding elemental mapping results indicate that the homogeneous elemental distribution across the whole NSS pellet on sodium (Na), antimony (Sb), and sulfur (S). After infiltrating the phase-transition polymer, a smooth surface is observed (**Figure 1g**) and micropores are filled with polymers, suggesting great contact between inorganic sulfide and polymer. Figure S6 displays the cross-sectional SEM image and EDS mapping of NSS/PPP SCE pellet, whereas the distributions of C, O elements from PPP polymer and Na, Sb, S elements from NSS are complementary.

The ionic conductivity of the prepared 3D-NSS/PPP SCE was evaluated. **Figure 2a** presents the Nyquist plots of the prepared 3D-NSS/PPP SCE at different temperatures, namely, 30, 50, 55, 70, and 80 °C. The Nyquist plots show a typical small semi-circle at high frequency and a steep linear spike at low frequency, which is a feature of fast solid ion conductors[18, 27]. The ionic conductivity of 3D-NSS/PPP SCE was calculated to be 8.2×10^{-5} S cm^{-1} and 2.3×10^{-4} S cm^{-1} at 30 and 55 °C, respectively. NSS sulfide has an ionic conductivity of 2.5×10^{-4} S

cm^{-1} at room temperature, which is more than 4 times higher than that of PPP/NaTFSI polymer electrolyte (6.1×10^{-5} S cm^{-1}). Considering such big differences on ionic conductivity and high portion of ceramic component (~68 wt%), the ion transport in 3D-NSS/PPP SCE is considered to mostly comes from ceramic instead of polymer component.[44] On the other hand, 3D porous NSS displays an ionic conductivity of 1.07×10^{-4} S cm^{-1} at room temperature (Figure S7), which is lower than that of dense NSS pellet due to the porous structure. The Arrhenius plots of 3D-NSS/PPP SCE, NSS pellet and PPP polymer electrolytes are shown in **Figure 2b**. As increasing temperature, the PPP polymer exhibits an abrupt increase on ionic conductivity due to the phase transition.[27] In contrast, 3D-NSS/PPP SCE shows a linear Arrhenius behavior with the activation energy determined to be 0.338 eV, higher than that of pure and dense NSS pellet (0.226 eV). The activation energy of NSS pellet is consistent with previous literatures,[10, 17, 27] confirming the tetragonal phase NSS. In addition, **Figure 2c** shows the polarization curve of 3D-NSS/PPP SCE to examine its transference number (t_{Na^+}) and the inset is the EIS measurements at initial and steady state. Fitting EIS plots allows to obtain the R_0 and R_{ss} values, corresponding to the resistance before and after polarization, respectively. The Na-ion transference number (t_{Na^+}) is further calculated to be 0.47 following Bruce-Vincent equation as explained in the experimental section.

The electrochemical stability of 3D-NSS/PPP SCE toward Na metal was studied in symmetric cells by sandwiching the SCE between two sodium foils for plating/striping process at room temperature. **Figure 2d** compares the cycling performance of Na symmetric cells with porous NSS pellet and 3D-NSS/PPP SCE under the current density of 0.1 mA cm^{-2} (area capacity of 0.05 mA h cm^{-2}). Despite the initial values are similar (0.2-0.3 V), the overpotential

of Na symmetric cell with porous NSS pellet continually increases to 0.5 V at the 3rd cycle (**Figure 2e**) and ultimately arrives to 2 V after 150 hours (**Figure 2f**). Notably, porous NSS pellet shows better cycling performance than the symmetric cell with dense pellet (Figure S8). In contrast, the cell with 3D-NSS/PPP SCE exhibits much flat and stable variation trend on the overpotential for 150 hours under a current density of 0.1 mA cm^{-2}, reflecting the excellent interface stability between the Na metal and 3D-NSS/PPP SCE. Moreover, the stable interface is further confirmed by the observation of constant impedance values in EIS measurement after different cycles for Na symmetric cell with 3D-NSS/PPP SCE (Figure S9). This trend is totally different with the increased impedance for Na|NSS pellet|Na and Na|3D-NSS|Na after different cycling cycles (Figure S10 and Figure S11). In addition, Na symmetric cell with 3D-NSS/PPP SCE under a higher current density (0.2 mA cm^{-2}) also displays a stable electrochemical cycling (Figure S12), indicating a stable interface. The CCD testing results of 3D-NSS/PPP SCE in Na symmetric cell (Figure S13) show that the polarization voltage continuedly increases as the current density rises, and the critical current density value for 3D-NSS/PPP SCE is estimated to be about 0.4 mA cm^{-2}. This value is close to that of 3D-NSS in Na symmetric cell (Figure S14), but lower than the Na|NSS|Na cell with 0.7 mA cm^{-2} (Figure S15).

To understand the interface after cycling, the cycled Na symmetric cells with pure NSS and 3D-NSS/PPP SCE were disassembled for XPS analysis. Figure S15 displays the XPS spectra for the cycled symmetric cells with pure NSS and 3D-NSS/PPP. After cycling in symmetric cell with pure NSS, a doublet from metallic Sb and another doublet attributed to Na_2S are observed in the spectra of Sb 3d and S 2p, which is different with the original Sb-S and Sb=S bonding in pristine NSS. This observation indicates that the interfacial reaction

between Na metal and NSS, consistent with previous observations.[19, 45] In contrast, for the cycled cell with 3D-NSS/PPP SCE, there are no obvious peaks from Sb-S, suggesting that PPP fully protect the surface of porous NSS and prohibit the interfacial reactions.

The cycling ability of 3D-NSS/PPP SCE was investigated in SSMBs using Na metal as the anode and metal sulfide (TiS_2 or FeS_2) as the active cathode. **Figure 3a** displays the dQ/dV plots of TiS_2|SCE|Na cells at different cycles (1^{st}, 2^{nd}, 5^{th}, 10^{th}). At the first few cycles, three pairs of anodic/cathodic peaks are clearly observed at 1.7/1.48, 2.2/2.06, and 2.3/2.1V, which are related with the Na^+ intercalation/deintercalation process in TiS_2 cathode. This observation is in great agreement with the electrochemical charge/discharge curves in the full cell (Figure S16) that display three obvious plateaus at 2.1, 2.2 V and 1.6 V, respectively. The first two peaks or plateaus can be attributed to the intercalation reaction of Na^+ into TiS_2 layers to produce Na_xTiS_2 with $0<x<0.4$, and the third peak/plateau corresponds to further intercalation process (Na_xTiS_2 with $0.4<x<0.8$).[46-49] As the cycling process proceeds, the peak positions are overlapped while the intensities obviously decrease (Figure S17).

The rate performance of SSMBs with structure of TiS_2|3D-NSS/PPP|Na under different current density (20-200 mA g^{-1}) is examined in **Figure 3b**. Under a low current density of 20 mA g^{-1}, the cell exhibits an initial discharge specific capacity of 207 mA h g^{-1}. The specific capacity values decline to 105 and 48 mA h g^{-1} as increasing the current density to 50 and 200 mA g^{-1}, respectively. After the current density returns to 20 mA g^{-1}, the specific capacity of SCE-based TiS_2||Na cell increases to 120 mA h g^{-1}, which is lower than the initial specific capacity due to the formation of irreversible phase (Na_xTiS_2) in TiS_2 cathode.[50] Nevertheless, the cycling results under different current densities (20-200 mA g^{-1}) and stably cycling for 60

more cycles after back to 20 mA g^{-1} indicate great rate performance for the cell with 3D-NSS/PPP SCE and TiS_2 cathode. **Figure 3c** shows the charge/discharge curves under different current densities, whereas obvious plateaus that corresponding to the Na^+ intercalation/deintercalation process can be clearly observed. Beside TiS_2, the SSMBs with FeS_2 cathode was also cycled under different current densities to study the rate performance. **Figure 3d** presents the charge/discharge curves of assembled FeS_2|3D-NSS/PPP SCE|Na that cycling under the current density from 20 to 200 mA g^{-1}. The cell exhibits a high specific discharge capacity of 350 mA h g^{-1} at 20 mA g^{-1}. When the current density increases to 50 and 100 mA g^{-1}, the specific capacity remains at 200 and 145 mA h g^{-1}, respectively. When the current density goes back to 20 mA g^{-1} after cycling at 200 mA g^{-1}, the specific capacity returns to 247 mA h g^{-1} (Figure S18).

The long-term cycling performance of SSMBs (TiS_2|3D-NSS/PPP SCE|Na) up to 500 cycles under a current density of 50 mA g^{-1} is displayed in **Figure 3e**. The cell delivers an initial specific discharge capacity of 176 mA h g^{-1}, which decreases to 134 and 121 mA h g^{-1} at the 10^{th} cycle and 20^{th} cycle, respectively. The capacity decay at the initial 20 cycles is possibly due to the formation of irreversible phase such as Na_xTiS_2 in TiS_2 cathode.[50] After 20 cycles, the cell exhibits stable cycling with high coulombic efficiency above 99.9%. The charge/discharge curves (Figure S16) show obvious plateaus for all cycles, corresponding electrochemical Na^+ insertion/extraction process to TiS_2 cathode. When using FeS_2 as cathode for SSMBs with 3D-NSS/PPP SCE, the cell exhibits a higher initial capacity of 328 mA h g^{-1} and flat plateaus at 1.22 V (Figure S19). Nevertheless, the specific capacity decreases to 120 and 90 mA h g^{-1} at the 50^{th} and 100^{th} cycle, respectively. Compared to the reported performance

of solid-state batteries with NSS-based electrolytes (Table S2), our solid-state Na||TiS_2 metal batteries with 3D-NSS/PPP SCE shows a long cycling stability of 550 cycles under a high current density (50 mA cm^{-2}).

In addition to metal sulfide (TiS_2 or FeS_2) cathode, the feasibility of 3D-NSS/PPP SCE pairing with high voltage oxide cathode was also investigated in SSMBs. Previous literatures report that the stable electrochemical window of pure NSS is around 1.5-2.35 V.[18, 51-52] The electrochemical window of NSS was measured by experiment. Due to the interfacial reaction between sodium metal and NSS,[19, 53-54] Na-Sn alloy was typically chosen as the stable anode in solid-state sodium batteries with NSS-based electrolytes.[55] Therefore, Na_2Sn (0.3 V vs. Na^+/Na)[56] was utilized as the reference electrode in LSV measurement. The decomposition voltage was measured to be 2.09 V (vs. Na^+/Na, 1.79 V vs. Na^+/Na_2Sn) according to Figure S20. Thus, NSS is incompatible with high voltage cathode unless applying a surface coating on cathode materials.[57-59] In the design of 3D-NSS/PPP SCE, the PPP polymer on the surface of 3D porous NSS framework provides the possibility to extend the electrochemical window of SCE. The LSV curve (**Figure 4a**) of Na|3D-NSS/PPP SCE|SS cell shows that the current dramatically increases after the voltage goes beyond 5V, suggesting that the decomposition voltage of SCE up to 5.65 V for a wider electrochemical window.

Using high voltage oxide P2-$Na_{0.67}Ni_{0.33}Mn_{0.67}O_2$ (NNMO) as cathode, SSMBs with Na anode and 3D-NSS/PPP SCE were assembled and tested in coin cells without additional pressure. **Figure 4b** displays the dQ/dV curves within the voltage range of 2-4 V. The differential curves show obvious anodic/ cathodic peaks at 3.19/3.08, 3.36/3.24, 3.65/3.53, 3.73/3.62V, respectively. These peak positions correspond to various steps of Na^+ intercalation

and deintercalation, in agreement with those Na-ion batteries using liquid electrolytes.[60] As the electrochemical cycling proceeds, the peaks' intensity slight decreases meanwhile their positions also shift. When cycling at 0.1 C, the NNMO|3D-NSS/PPP SCE|Na cell exhibits a specific discharge capacity of 82 mA h g^{-1} (**Figure 4c**). As expected, the specific capacity obviously decreases as increasing the C-rate (0.2, 0.5, 0.75 and 1 C in **Figure 4d**). This observation is different from the cycling behaviors of NNMO cathode in the cell with liquid electrolyte,[61] which is possible due to the slow ion transport in the SSMBs. After returning to 0.1 C, the specific capacity resumes back to 80 mA h g^{-1} while accompanies with fast capacity decay. The low capacity retain is considered with the strong reaction at interface, which will be investigated in our future work. To further understand the interface stability, the cycled NNMO|3D-NSS/PPP|Na battery was disassembled for XPS characterization. As shown in Figure S21, the pristine NNMO displays the obvious Ni 2p and Mn 2p peaks from active cathode as well as the C-O, C-C, F-C-F peaks from carbon and PVDF. In contrast, after cycling, the PPP from SCE covers the cathode surface, which blocking the signals of Mn, Ni of NNMO cathode. Furthermore, 3D ToF-SIMS chemical imaging the spatial distributions for the cycled NNMO cathode displays the increased intensity for Ni^+ and Mn^+ secondary ions as increasing the depth (Figure S23).

When pairing with 3D-NSS/PPP SCE in solid-state Na metal batteries, TiS_2 cathode displays the longest cycling stability up to 550 cycles although the initial specific capacity is relatively low (176 mA h g^{-1}). The high cycling stability is considered to relate with the layer structure of TiS_2.[46, 48] In comparison, FeS_2 cathode shows high specific capacity of 328 mA h g^{-1} at the same current density within an electrochemical voltage window (0.9-3.0 V), which is

related with high theoretical capacity for FeS_2.[62-63] On the other hand, with NNMO cathode at a higher voltage (2.0-4.0 V), the cell exhibits obvious discharge/charge plateaus and anodic/cathodic peaks, while the cycling stability is not as good as those cells with transition metal sulfides.

Regarding the interface between SE and metal anode, there are three interphase models[64]: 1) thermodynamically and electrochemically stable; 2) a stable interphase that good at ion transport and insulate for electrons; 3) an interphase with both ionic and electronic conductivity. The former two results in a stable interface while the last one causes interfacial reaction. The case of NSS and Na metal belongs to the third one, which has been reported in previous literatures. To address such interface instability, different approaches have been attempted, including Na-Sn alloy anode,[65-66] halide-doped sulfide solid electrolytes,[24, 67] as well as the artificial interlayer between SE and Na metal.[19, 53] In this work, the infiltrated PPP/NaTFSI in 3D-NSS not only plays a role for Na-ion transport, but also acts as an efficient interlayer to improve the interface contact between NSS and electrode as well as increase the electrochemical stability.

4. Conclusion

In summary, we prepared a self-templated 3D-NSS/PPP SCE through using a porous NSS framework as template to infiltrate PPP/NaTFSI polymer electrolyte, with the NSS weight content of 68%. The 3D-NSS/PPP SCE exhibited obvious improvement at interface stability toward Na metal in symmetric cells, which show flat and stable overpotential profiles. The TiS_2|3D-NSS/PPP SCE|Na SSMBs delivered an initial specific capacity of 170 mA h g^{-1} and a

long-term cyclability up to 550 cycles under a current density of 50 mA h g^{-1}. When using FeS_2 as cathode, the cell with 3D-NSS/PPP SCE showed an initial capacity of 350 mA h g^{-1} at a current density of 20 mA h g^{-1}. In addition, the feasibility of 3D-NSS/PPP SCE pairing with oxide cathode ($Na_{0.67}Ni_{0.33}Mn_{0.67}O_2$) in SSMBs was also demonstrated with a specific capacity of 80 mA h g^{-1} at 0.1C. This research provides a feasible approach to prepare sulfide-rich SCE via a self-template method, advancing the development of solid-state sodium batteries.

Acknowledgement

The authors thank the support from U.S. National Science Foundation Award (No. 2047460). We also acknowledge the support from the Conn Center for Renewable Energy Research at University of Louisville. K. Graff and H. Xiong acknowledge the support from National Science Foundation Award (DUE–2111549) and U.S. Department of Energy, Office of Science, Office of Basic Energy Sciences program under Award Number DE-SC0019121.

CRediT authorship contribution statement.

Xiaolin Guo: Conceptualization, Methodology, Formal analysis, Investigation, Visualization, Writing-original draft; **Yang Li**: Investigation, Writing-review & editing; **Selim Halacoglu**: Formal analysis, Methodology, Investigation, Writing-review & editing; **Kincaid Graff**: Methodology, Formal analysis, Investigation, Writing-review & editing; **Kelvin Fu:** Methodology, Investigation, Writing-review & editing; **Claire(Hui) Xiong**: Methodology, Investigation, Funding acquisition, Writing-original draft, Writing-review & editing; **Hui Wang**: Conceptualization, Methodology, Investigation, Funding acquisition, Writing-original draft, Writing-review & editing.

Reference

[1] C. Zhao, L. Liu, X. Qi, Y. Lu, F. Wu, J. Zhao, Y. Yu, Y. S. Hu, L. Chen, *Adv. Energy Mater.* **2018**, 8.

[2] P. K. Nayak, L. Yang, W. Brehm, P. Adelhelm, *Angew Chem Int Ed Engl* **2018**, 57, 102.

[3] E. Jin, J. Su, H. Hou, P. Pirayesh, Y. Wang, Y. Yuan, H. Yan, G. Popov, L. V. Goncharova, S. Ketabi, *Adv. Mater.* **2024**, 2406837.

[4] P. Pirayesh, E. Jin, Y. Wang, Y. Zhao, *Energy & Environmental Science* **2023**.

[5] M. Li, C. Sun, X. Yuan, Y. Li, Y. Yuan, H. Jin, J. Lu, Y. Zhao, *Adv. Funct. Mater.* **2024**, 34, 2314019.

[6] R. Collongues, D. Gourier, A. Kahn, J. P. Boilot, P. Colomban, A. Wicker, *J. Phys. Chem. Solids* **1984**, 45, 33.

[7] Y. Li, C. Sun, Z. Sun, M. Li, H. Jin, Y. Zhao, *Adv. Funct. Mater.* 2403937.

[8] R. DeWees, H. Wang, *ChemSusChem* **2019**, 12, 3713.

[9] A. Hayashi, K. Noi, A. Sakuda, M. Tatsumisago, *Nat Commun* **2012**, 3, 856.

[10] H. Wang, Y. Chen, Z. D. Hood, G. Sahu, A. S. Pandian, J. K. Keum, K. An, C. Liang, *Angew Chem Int Ed Engl* **2016**, 55, 8551.

[11] M. Duchardt, U. Ruschewitz, S. Adams, S. Dehnen, B. Roling, *Angew Chem Int Ed Engl* **2018**, 57, 1351.

[12] E. A. Wu, S. Banerjee, H. Tang, P. M. Richardson, J. M. Doux, J. Qi, Z. Zhu, A. Grenier, Y. Li, E. Zhao, G. Deysher, E. Sebti, H. Nguyen, R. Stephens, G. Verbist, K. W. Chapman, R. J. Clement, A. Banerjee, Y. S. Meng, S. P. Ong, *Nat Commun* **2021**, 12, 1256.

[13] J. Liu, S. Wang, Y. Kawazoe, Q. Sun, *ACS Materials Letters* **2023**, 5, 1009.

[14] R. Schlem, A. Banik, M. Eckardt, M. Zobel, W. G. Zeier, *ACS Applied Energy Materials* **2020**, 3, 10164.

[15] H. Jia, L. Peng, C. Yu, L. Dong, S. Cheng, J. Xie, *Journal of Materials Chemistry A* **2021**, 9, 5134.

[16] D. Zhang, X. Cao, D. Xu, N. Wang, C. Yu, W. Hu, X. Yan, J. Mi, B. Wen, L. Wang, L. Zhang, *Electrochimica Acta* **2018**, 259, 100.

[17] A. Banerjee, K. H. Park, J. W. Heo, Y. J. Nam, C. K. Moon, S. M. Oh, S. T. Hong, Y. S. Jung, *Angew Chem Int Ed Engl* **2016**, 55, 9634.

[18] S. Halacoglu, Y. Li, W. Arnold, V. Shreyas, X. Guo, J. B. Jasinski, B. Narayanan, H. Wang, *Chemical Engineering Journal* **2023**, 468.

[19] P. Hu, Y. Zhang, X. Chi, K. Kumar Rao, F. Hao, H. Dong, F. Guo, Y. Ren, L. C. Grabow, Y. Yao, *ACS Appl Mater Interfaces* **2019**, 11, 9672.

[20] S. Zhang, Y. Zhao, F. Zhao, L. Zhang, C. Wang, X. Li, J. Liang, W. Li, Q. Sun, C. Yu, J. Luo, K. Doyle‐Davis, R. Li, T. K. Sham, X. Sun, *Adv. Funct. Mater.* **2020**, 30.

[21] Q. Ni, Y. Xiong, Z. Sun, C. Sun, Y. Li, X. Yuan, H. Jin, Y. Zhao, *Adv. Energy Mater.* **2023**, 13, 2300271.

[22] Y. Zhao, C. Wang, Y. Dai, H. Jin, *Nano Energy* **2021**, 88, 106293.

[23] X. Guo, S. Halacoglu, Y. Chen, H. Wang, *Small* **2024**, 2311195.

[24] H. Cao, M. Yu, L. Zhang, Z. Zhang, X. Yan, P. Li, C. Yu, *Journal of Materials Science & Technology* **2021**, 70, 168.

[25] L. Yu, J. Yin, C. Gao, C. Lin, X. Shen, S. Dai, Q. Jiao, *ACS Applied Materials & Interfaces* **2023**, 15, 31635.

[26] S. Zhang, Y. Zhao, F. Zhao, L. Zhang, C. Wang, X. Li, J. Liang, W. Li, Q. Sun, C. Yu, J. Luo, K. Doyle-Davis, R. Li, T.-K. Sham, X. Sun, *Adv. Funct. Mater.* **2020**, 30, 2001118.

[27] Y. Li, W. Arnold, S. Halacoglu, J. B. Jasinski, T. Druffel, H. Wang, *Adv. Funct. Mater.* **2021**, 31.

[28] Z. L. Dong, Y. Yuan, V. Martins, E. Jin, Y. Gan, X. Lin, Y. Gao, X. Hao, Y. Guan, J. Fu, X. Pang, Y.

Huang, Q. H. Tu, T.-K. Sham, Y. Zhao, *Nano Energy* **2024**, 128.
[29] X. Guo, Y. Li, H. Wang, *ACS Applied Energy Materials* **2024**, 7, 1008.
[30] H. Huo, Y. Chen, J. Luo, X. Yang, X. Guo, X. Sun, *Adv. Energy Mater.* **2019**, 9.
[31] L. Chen, Y. Li, S.-P. Li, L.-Z. Fan, C.-W. Nan, J. B. Goodenough, *Nano Energy* **2018**, 46, 176.
[32] Y. Li, W. Arnold, A. Thapa, J. B. Jasinski, G. Sumanasekera, M. Sunkara, T. Druffel, H. Wang, *ACS Appl Mater Interfaces* **2020**, 12, 42653.
[33] C. Wang, R. Yu, H. Duan, Q. Lu, Q. Li, K. R. Adair, D. Bao, Y. Liu, R. Yang, J. Wang, S. Zhao, H. Huang, X. Sun, *ACS Energy Letters* **2021**, 7, 410.
[34] Z. Zhang, L. Wu, D. Zhou, W. Weng, X. Yao, *Nano Lett* **2021**, 21, 5233.
[35] Y. Wang, J. Ju, S. Dong, Y. Yan, F. Jiang, L. Cui, Q. Wang, X. Han, G. Cui, *Adv. Funct. Mater.* **2021**, 31.
[36] Y. Yan, J. Ju, S. Dong, Y. Wang, L. Huang, L. Cui, F. Jiang, Q. Wang, Y. Zhang, G. Cui, *Adv Sci (Weinh)* **2021**, 8, 2003887.
[37] J. Bae, Y. Li, J. Zhang, X. Zhou, F. Zhao, Y. Shi, J. B. Goodenough, G. Yu, *Angew Chem Int Ed Engl* **2018**, 57, 2096.
[38] H. Wang, Y. Chen, Z. D. Hood, G. Sahu, A. S. Pandian, J. K. Keum, K. An, C. Liang, *Angewandte Chemie* **2016**, 128, 8693.
[39] D. Hou, E. Gabriel, K. Graff, T. Li, Y. Ren, Z. Wang, Y. Liu, H. Xiong, *Journal of Materials Research* **2022**, 37, 1156.
[40] S. Halacoglu, Y. Li, W. Arnold, V. Shreyas, X. Guo, J. B. Jasinski, B. Narayanan, H. Wang, *Chemical Engineering Journal* **2023**, 468, 143624.
[41] S. Dong, G. Xie, S. Xu, X. Tan, M. Chaudhary, Y. Zhang, R. Wu, F. Wen, C. Ayranci, V. K. Michaelis, A. Quirk, S. M. Rosendahl, J. Liu, M. D. Fleischauer, L. Sang, *ACS Nano* **2024**, 18, 16285.
[42] Y. Fu, Z. Gong, D. Li, Y. Liu, X. Zhou, Y. Yang, Q. Jiao, *Journal of Materials Science* **2024**, 59, 3009.
[43] B. Tang, Y. Zhao, Z. Wang, S. Chen, Y. Wu, Y. Tseng, L. Li, Y. Guo, Z. Zhou, S.-H. Bo, *eScience* **2021**, 1, 194.
[44] J. Zheng, M. Tang, Y.-Y. Hu, *Angewandte Chemie International Edition* **2016**, 55, 12538.
[45] E. A. Wu, C. S. Kompella, Z. Zhu, J. Z. Lee, S. C. Lee, I.-H. Chu, H. Nguyen, S. P. Ong, A. Banerjee, Y. S. Meng, *ACS Applied Materials & Interfaces* **2018**, 10, 10076.
[46] Z. Hu, Z. Tai, Q. Liu, S. W. Wang, H. Jin, S. Wang, W. Lai, M. Chen, L. Li, L. Chen, *Adv. Energy Mater.* **2019**, 9, 1803210.
[47] G. H. Newman, L. P. Klemann, *Journal of The Electrochemical Society* **1980**, 127, 2097.
[48] A. Chaturvedi, E. Edison, N. Arun, P. Hu, C. Kloc, V. Aravindan, S. Madhavi, *ChemistrySelect* **2018**, 3, 524.
[49] H.-S. Ryu, J.-S. Kim, J.-S. Park, J.-W. Park, K.-W. Kim, J.-H. Ahn, T.-H. Nam, G. Wang, H.-J. Ahn, *Journal of the Electrochemical Society* **2012**, 160, A338.
[50] H.-S. Ryu, J.-S. Kim, J.-S. Park, J.-W. Park, K.-W. Kim, J.-H. Ahn, T.-H. Nam, G. Wang, H.-J. Ahn, *Journal of The Electrochemical Society* **2012**, 160, A338.
[51] Z. Zhu, H. Tang, J. Qi, X. G. Li, S. P. Ong, *Adv. Energy Mater.* **2021**, 11.
[52] R. Jalem, B. Gao, H.-K. Tian, Y. Tateyama, *Journal of Materials Chemistry A* **2022**, 10, 2235.
[53] Y. Li, S. Halacoglu, V. Shreyas, W. Arnold, X. Guo, Q. Dou, J. B. Jasinski, B. Narayanan, H. Wang, *Chemical Engineering Journal* **2022**, 434, 134679.
[54] G. Xie, M. Tang, S. Xu, A. Brown, L. Sang, *ACS Applied Materials & Interfaces* **2022**, 14, 48705.
[55] T. W. Kim, K. H. Park, Y. E. Choi, J. Y. Lee, Y. S. Jung, *Journal of Materials Chemistry A* **2018**, 6, 840.
[56] E. A. Wu, S. Banerjee, H. Tang, P. M. Richardson, J.-M. Doux, J. Qi, Z. Zhu, A. Grenier, Y. Li, E. Zhao,

Nature communications **2021**, 12, 1256.
[57] N. Ohta, K. Takada, I. Sakaguchi, L. Zhang, R. Ma, K. Fukuda, M. Osada, T. Sasaki, *Electrochemistry Communications* **2007**, 9, 1486.
[58] J. Park, J. P. Son, W. Ko, J.-S. Kim, Y. Choi, H. Kim, H. Kwak, D.-H. Seo, J. Kim, Y. S. Jung, *ACS Energy Letters* **2022**, 7, 3293.
[59] K. Wang, Z. Liang, S. Weng, Y. Ding, Y. Su, Y. Wu, H. Zhong, A. Fu, Y. Sun, M. Luo, J. Yan, X. Wang, Y. Yang, *ACS Energy Letters* **2023**, 8, 3450.
[60] Y. Xie, E. Gabriel, L. Fan, I. Hwang, X. Li, H. Zhu, Y. Ren, C. Sun, J. Pipkin, M. Dustin, M. Li, Z. Chen, E. Lee, H. Xiong, *Chem Mater* **2021**, 33, 4445.
[61] H. Wang, B. Yang, X.-Z. Liao, J. Xu, D. Yang, Y.-S. He, Z.-F. Ma, *Electrochimica Acta* **2013**, 113, 200.
[62] Z. Lu, Y. Zhai, N. Wang, Y. Zhang, P. Xue, M. Guo, B. Tang, D. Huang, W. Wang, Z. Bai, *Chemical Engineering Journal* **2020**, 380, 122455.
[63] W. Chen, S. Qi, M. Yu, X. Feng, S. Cui, J. Zhang, L. Mi, *Electrochimica Acta* **2017**, 230, 1.
[64] S. Wenzel, T. Leichtweiss, D. A. Weber, J. Sann, W. G. Zeier, J. Janek, *ACS Applied Materials & Interfaces* **2016**, 8, 28216.
[65] H. Gamo, N. H. H. Phuc, R. Matsuda, H. Muto, A. Matsuda, *Materials Today Energy* **2019**, 13, 45.
[66] T. Ando, A. Sakuda, M. Tatsumisago, A. Hayashi, *Electrochemistry Communications* **2020**, 116, 106741.
[67] I.-H. Chu, C. S. Kompella, H. Nguyen, Z. Zhu, S. Hy, Z. Deng, Y. S. Meng, S. P. Ong, *Scientific Reports* **2016**, 6, 33733.

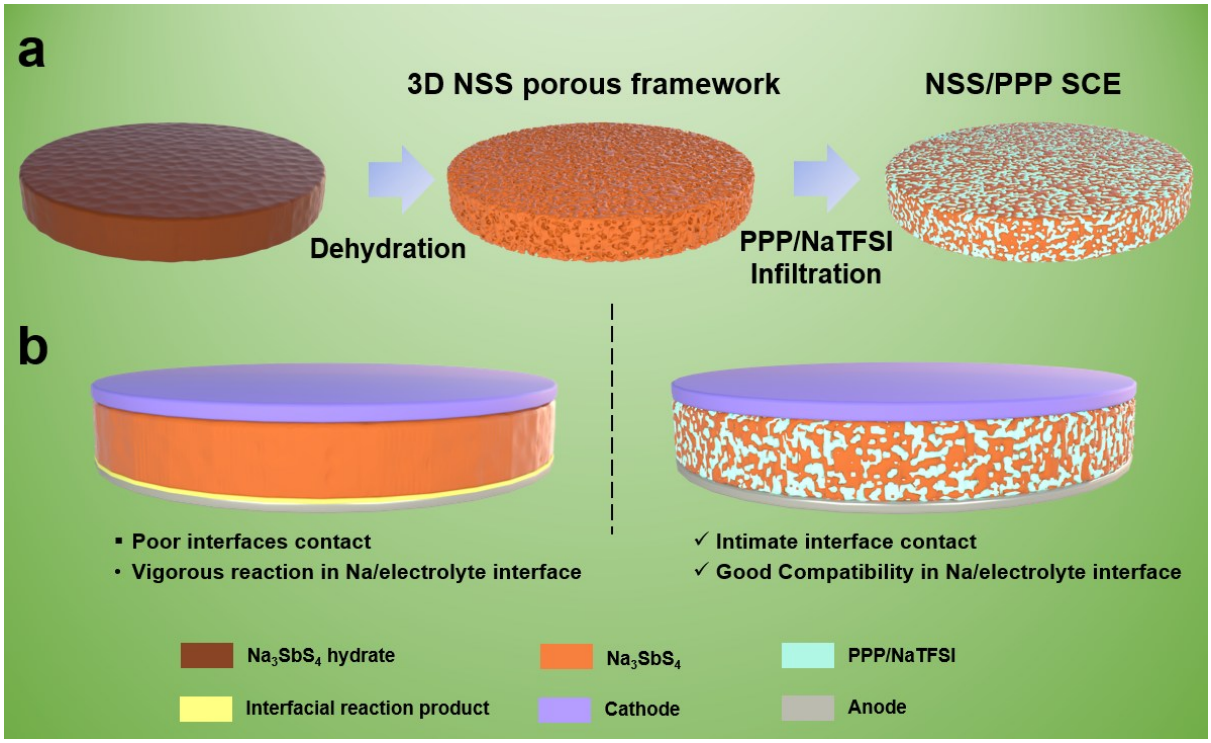

Scheme 1. (a) Synthesis process of 3D porous Na_3SbS_4/PPP SCE by self-template method. (b) Comparison of full battery assembly using 3D porous NSS and 3D structured Na_3SbS_4/PPP SCE.

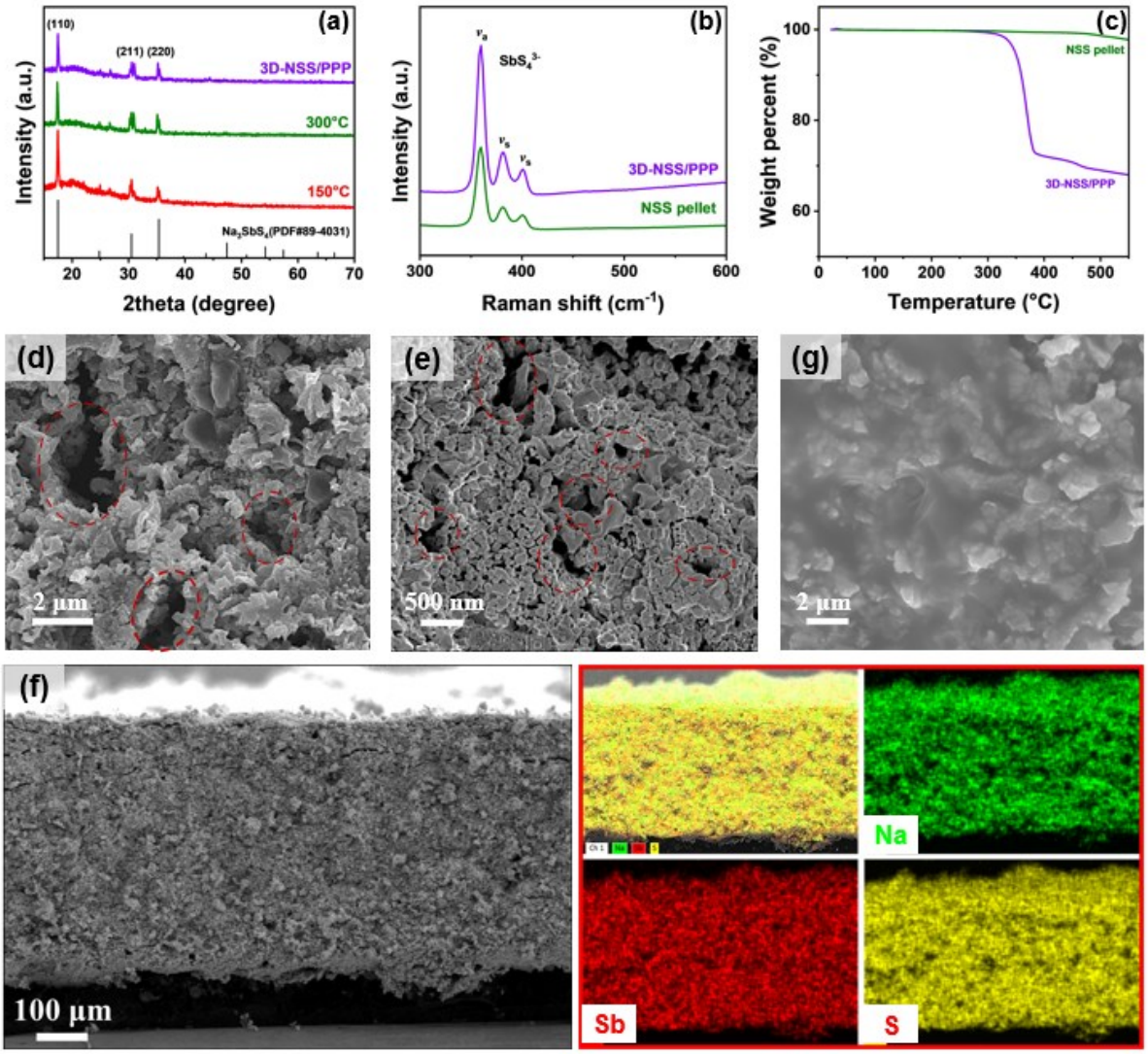

Figure 1. (a) XRD patterns, (b) Raman spectra (c) TGA curves of heat-treated NSS pellet and 3D-NSS/PPP SCE; Surface SEM images of (d) (e) 3D porous Na_3SbS_4 and (f) cross-sectional SEM image of 3D porous NSS pellet, and the corresponding elemental mapping of sodium (Na), antimony (Sb) and sulfur (S). (g) SEM image of 3D-NSS/PPP SCE.

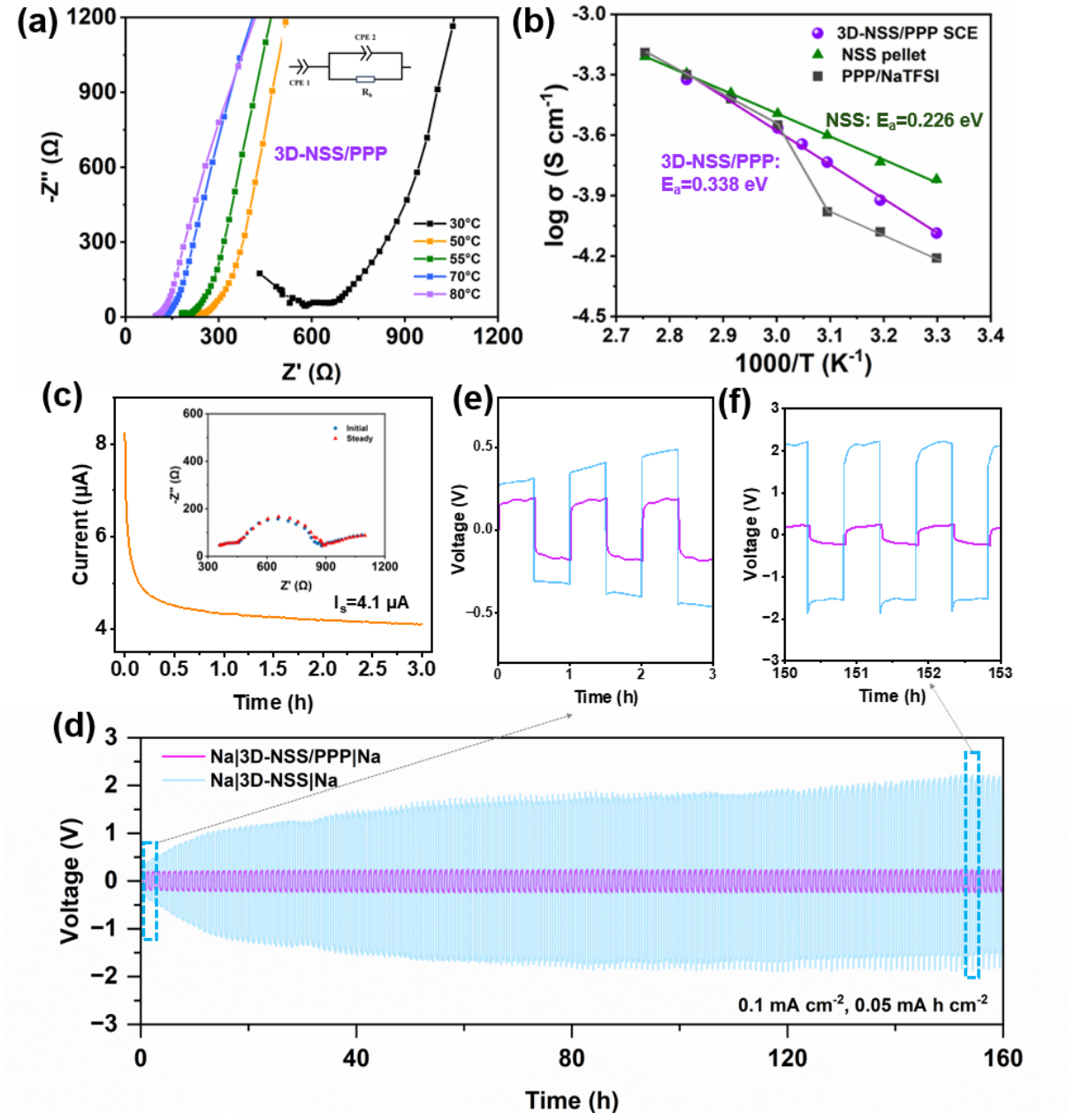

Figure 2. (a) Nyquist plots at different temperatures and inset is the equivalent circuit model. (b) Arrhenius plot of 3D-NSS/PPP SCE within 30-80 °C. (c) the variation of current with time for the symmetric cell (Na|3D-NSS/PPP SCE|Na) under the polarization of 10 mV. Inset shows the electrochemical impedance spectroscopy of symmetric cell before and after the polarization. (d) cycling performance of Na symmetric cells with porous NSS pellet and 3D-NSS/PPP SCE; enlarged profiles of (d) at different cycles (e) 0-3 hours, (f) 150-153 hours.

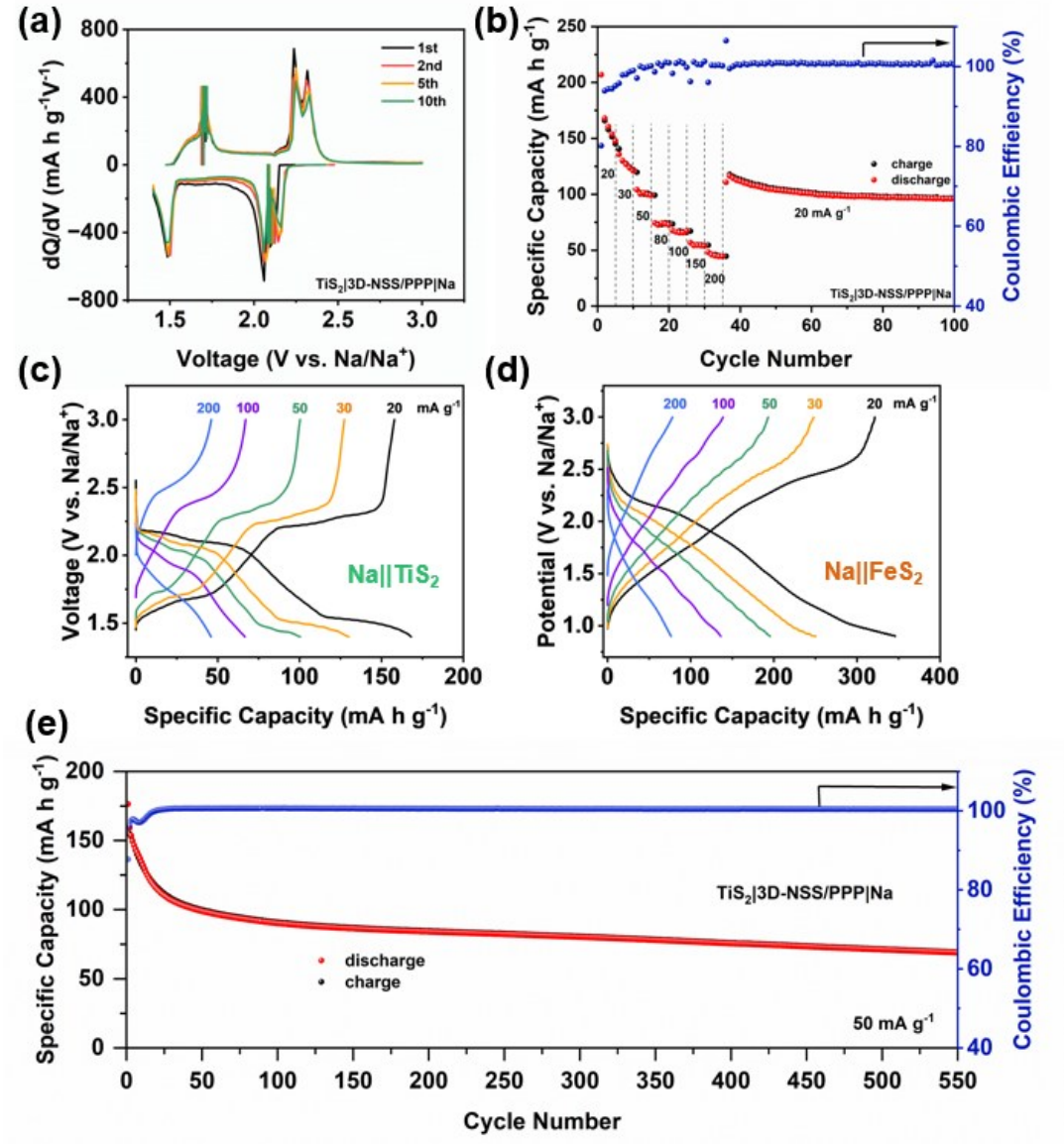

Figure 3. Electrochemical measurements of SSMBs with Na metal and 3D-NSS/PPP SCE: (a) the dQ/dV profiles at different cycles (1st, 2nd, 5th, 10th), (b) rate performance cycling under different current densities (20, 30, 50, 80, 100, 150, 200 mA h g^{-1}, then back to 20 mA h g^{-1}), (c) charge/discharge profiles at the current densities of 20, 30, 50, 100, 200 mA h g^{-1} for the cell with TiS_2 cathode; (d) the charge and discharge profiles for FeS_2||Na SSMBs with 3D-NSS/PPP SCE; (e) long-term cycling performance of TiS_2|3D-NSS/PPP SCE|Na at the current density of 50 mA g^{-1}. (All the electrochemical battery cycling of SSMBs is at 55 °C).

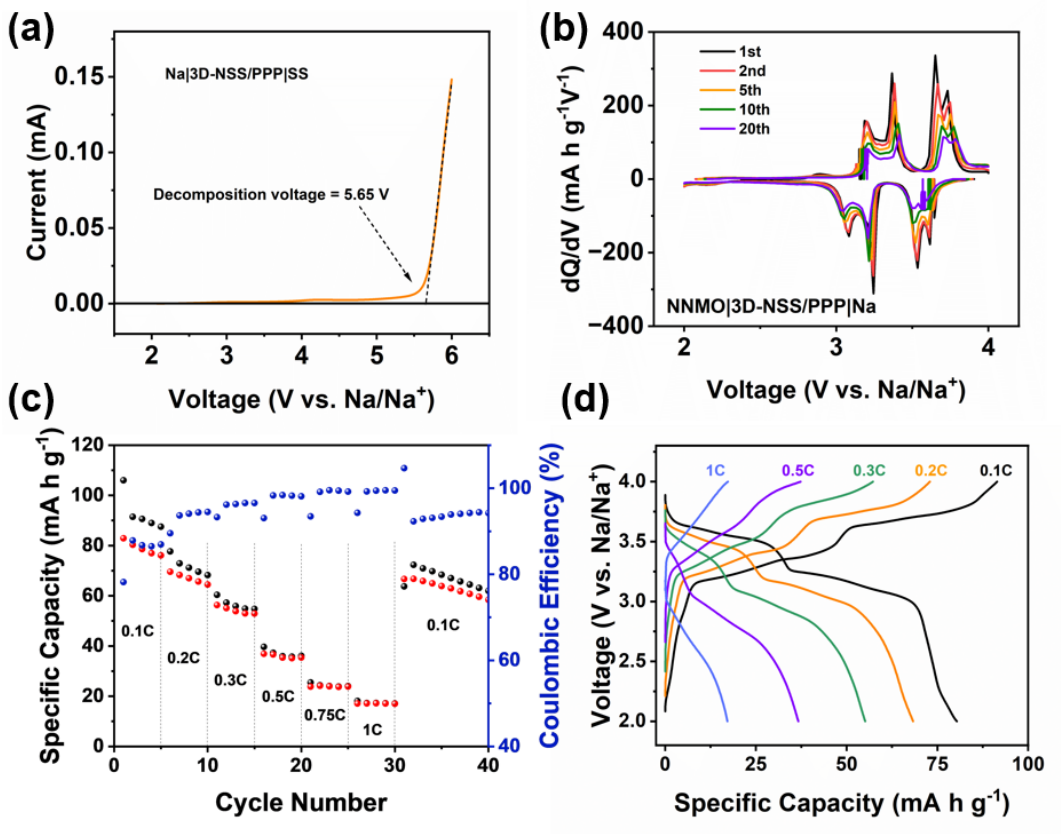

Figure 4. (a) Linear sweeping voltammetry test of Na|3D-NSS/PPP|stainless steel. The scan rate is 1 mV s^{-1}. The electrochemical performance of P2-$Na_{0.67}Ni_{0.33}Mn_{0.67}O_2$ (NNMO)|3D-NSS/PPP|Na. (b) the differential capacity curves of NNMO|3D-NSS/PPP|Na at different cycles, (c) the rate performance at the current density of 0.1, 0.2, 0.3, 0.5, 0.75 and 1C, respectively, (d) the corresponding charge/discharge profiles at the current densities of 0.1, 0.2, 0.3, 0.5, 1C, respectively. (The battery cycling of SSMBs was under 55 °C).